

A Machine Learning Tool to Analyse Spectroscopic Changes in High-Dimensional Data

Alberto Martinez-Serra^{1†}, Gionni Marchetti^{2,3†},
Francesco D'Amico⁴, Ivana Fenoglio⁵, Barbara Rossi⁴,
Marco P. Monopoli^{1*}, Giancarlo Franzese^{2,3*}

¹Department of Chemistry, Royal College of Surgeons in Ireland (RCSI),
University of Medicine and Health Sciences, 123 St Stephen's Green,
Dublin, D02 YN77, Ireland.

²Secció de Física Estadística i Interdisciplinària - Departament de Física
de la Matèria Condensada, Universitat de Barcelona, Martí i Franquès 1,
Barcelona, 08028, Spain.

³Institut de Nanociència i Nanotecnologia, Universitat de Barcelona,
Diagonal 645, Barcelona, 08028, Spain.

⁴Elettra Sincrotrone Trieste, S.S. 114 km 163.5, Basovizza, 34149 Trieste,
Italy.

⁵Department of Chemistry, University of Turin, Via Pietro Giuria 7,
10125 Turin, Italy.

*Corresponding author(s). E-mail(s): marcomonopoli@rcsi.com;
gfranzese@ub.edu;

Contributing authors: amartinezserra@rcsi.com; gionnimarchetti@ub.edu;
francesco.damico@elettra.eu; ivana.fenoglio@unito.it;
barbara.rossi@elettra.eu;

[†]These authors contributed equally to this work.

Abstract

When nanoparticles (NPs) are introduced into a biological solution, layers of biomolecules form on their surface, creating a corona. Understanding how the protein's structure evolves into the corona is essential for evaluating the safety and toxicity of nanotechnology. However, the influence of NP properties on protein conformation is not well understood. In this study, we propose a new method that addresses this issue by analyzing multi-component spectral data using

machine learning (ML). We apply the method to fibrinogen, a crucial protein in human blood plasma, at physiological concentrations while interacting with hydrophobic carbon or hydrophilic silicon dioxide NPs, revealing striking differences in the temperature dependence of the protein structure between the two cases. Our unsupervised ML method a) does not suffer from the challenges associated with the *curse of dimensionality*, and b) simultaneously handles spectral data from various sources. The method offers a quantitative analysis of protein structural changes upon adsorption and enhances the understanding of the correlation between protein structure and NP interactions, which could support the development of nanomedical tools to treat various conditions.

Keywords: Unsupervised Machine Learning, Manifold Reduction, Similarity Metrics, Clustering, Protein Structure, Biomolecular Corona, Spectroscopy, Hydrophobic Nanoparticles, Hydrophilic Nanoparticles

1 Introduction

Nanoparticles (NPs) are revolutionizing various scientific fields, from medicine to environmental science, due to their unique physical and chemical properties. As these particles interact with biological systems, understanding their behavior at the molecular level becomes crucial [1]. There is considerable experimental evidence that the NPs’ penetration of biological barriers—such as the blood-brain barrier, the intestines, and the lungs—is an active process that depends on the composition of the external biological solution and the biomolecular corona that forms as a result of the bio-nano interactions [2]. This surprising dependence clearly distinguishes nanomaterials (NMs) from chemical molecules [3]. Indeed, proteins, glycans, and lipids adhere so strongly to the NP surface that the exchange times with the solution are extremely long. Consequently, the biological identity of the particles depends mainly on the bio-corona instead of the NP chemistry itself [4].

Within the main constituents of the corona formed when NPs are exposed to human plasma, we find Fibrinogen (Fib) [5], one of the most abundant glycoproteins in human blood plasma with a concentration of about 1.5–4 g/L [6]. Synthesized in the liver by hepatocytes, it is essential for the coagulation cascade and also plays a significant role in blood viscosity, blood flow, and various other biological functions [7]. During the last decades, many studies have focused on the correlation of unusually elevated levels of Fib with an increased risk of experiencing health disorders, such as cardiovascular diseases [6].

Human Fib is formed by three polypeptide chains known as α , β , and γ chains, which remain linked by disulfide bonds in the terminal domains (Fig. 1). Their respective molecular masses are approximately 66.5, 52.0, and 46.5 kDa. The β and γ chains have two outer D domains or nodules, which connect to a central E domain through an alpha-helix segment. Along with the co- and post-translational N-linked carbohydrates added to the β and γ chains, the protein has a total molecular mass of around 340 kDa [8]. The domains at the extremes of the Fib structure are essential for understanding the biological role of the molecule in the human body. They enclose several

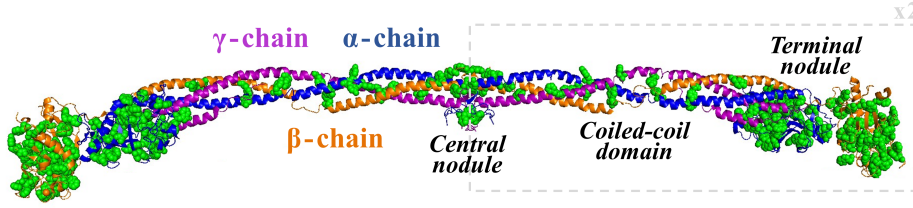


Fig. 1: 3D structure of Fib with atomic resolution determined by X-ray crystallography (PDB Entry: 3GHG). Different colors represent the various polypeptide chains of Fib: the α (blue), β (orange), and γ (pink) chains. It is a symmetric protein, with chains joined together at the central node, and terminal nodes for the β and γ chains. The aromatic amino acids are represented as green spheres and are mostly located in the terminal nodules, also in the central node, and much less in the alpha-helix.

binding sites that are involved in crucial processes, such as Fib conversion to fibrin and its cross-linking [9]. The α chain lacks these terminal nodules and essentially folds the other two chains, providing stability to the 3D structure.

Theoretical studies rationalized the non-monotonic behavior of the amount of competing proteins adsorbed on a surface in contact with blood plasma as a function of contact time and plasma concentration [10], with predictions at the molecular level confirmed by recent experiments [11]. In particular, understanding how the corona evolves and changes over time-dependent environmental conditions is fundamental in nanotoxicology and nanomedicine [12].

However, the way the NP surface influences the protein structural changes within the corona remains debated [13–16]. For instance, theory predicts that proteins near a hydrophobic interface should unfold and aggregate less than those in bulk, and that increasing temperature does not facilitate unfolding and reduces aggregation [17]. Conversely, on a hydrophilic NP, the prediction is that proteins adsorb while remaining folded, and as temperature increases, they unfold but do not desorb [18].

Here, by combining different experimental techniques with Machine Learning (ML) analysis, we characterize the structural changes in Fib over temperature when exposed to hydrophobic carbon NPs (CNP) and hydrophilic silicon dioxide (SiO_2) NPs. We employ several spectroscopic techniques: UltraViolet Resonance Raman (UVR) spectroscopy [19], Circular Dichroism (CD) [20], and UV absorption [21] spectroscopy.

All these techniques are non-destructive and do not require chemical labeling. For instance, by setting the excitation wavelength in UVR to the deep UV region (226 nm), the Raman signals associated with aromatic amino acids, such as tryptophan (Trp) and tyrosine (Tyr), are selectively enhanced, providing insights into the protein’s tertiary structure and how its chromophores interact with their surroundings [22, 23]. On the other hand, CD spectroscopy, which is based on the differential absorption of left- and right-hand circularly polarized light, can indicate the presence of disorder in the protein’s secondary structure [24, 25]. Lastly, UV absorption spectra are very

sensitive to the presence of aggregates and precipitates, which can elastically scatter light according to Rayleigh’s law [19].

We analyze our high-dimensional, multi-component data from various spectroscopic techniques using a novel unsupervised ML workflow designed to quantify and visualize how protein conformational changes occur as temperature varies. The novelty of our proposed ML model rests on two key algorithms: the Wasserstein distance [26, 27] and t-distributed stochastic neighbor embedding (t-SNE) [28–30].

These statistical tools are particularly advantageous because both remain unaffected by the *curse of dimensionality*, i.e., the challenges and limitations of working with high-dimensional data, such as overfitting, sparse distribution, computational complexity, and saturation of distances [31–33]. Indeed, high-dimensional data render standard similarity tools, such as the Euclidean and Manhattan distances commonly used in cheminformatics [34], ineffective.

Furthermore, t-SNE successfully replaces principal component analysis (PCA) [31, 35, 36], which is routinely employed to visualize spectral data in two-dimensional space. PCA cannot effectively handle data from diverse sources, mainly because, by preserving large distances arising from different spectra, it misses interesting structures, such as clustering, at smaller distances¹. In contrast, t-SNE overcomes this issue. When PCA is used as an initialization step, t-SNE can preserve both global and local data structures, yielding a meaningful embedding [30, 37].

Our multi-component data are organized into vectors with 856 dimensions, measured between 22 and 86°C at temperature intervals of $\Delta T = 4^\circ\text{C}$. Overall, our analysis reveals that the protein structural disorder gradually increases for Fib adsorbed onto CNPs as the temperature T rises, suggesting a ‘frozen’ partially unfolded structure that is only weakly dependent on T . In contrast, the structural behavior for Fib adsorbed onto SiO₂NPs is similar to that of free Fib, both characterized by a significant increase in disorder around 50°C. These findings are further supported by the t-SNE cluster analysis. For free Fib, the substantial increase in disorder is experimentally understood as a direct result of Fib aggregation. Therefore, our novel ML analysis of multi-component spectral data offers an experimental confirmation of theoretical predictions, providing insights into the interaction mechanisms between proteins and NPs. It highlights the importance of NP surface properties in protein adsorption and stability, and represents a new and solid method to analyze the controversial structural changes during biomolecular corona evolution.

2 Results

2.1 Experimental results

2.1.1 NP characterisation by Dynamic Light Scattering and Transmission Electron Microscopy and Fib corona stability

We follow the experimental protocols developed in our lab to obtain the protein corona complexes formed on top of carbon and silica NPs [38]. We first characterize the pristine NPs by Transmission Electron Microscope (TEM). By using an electron beam to

¹This is why PCA is susceptible to outliers in the data

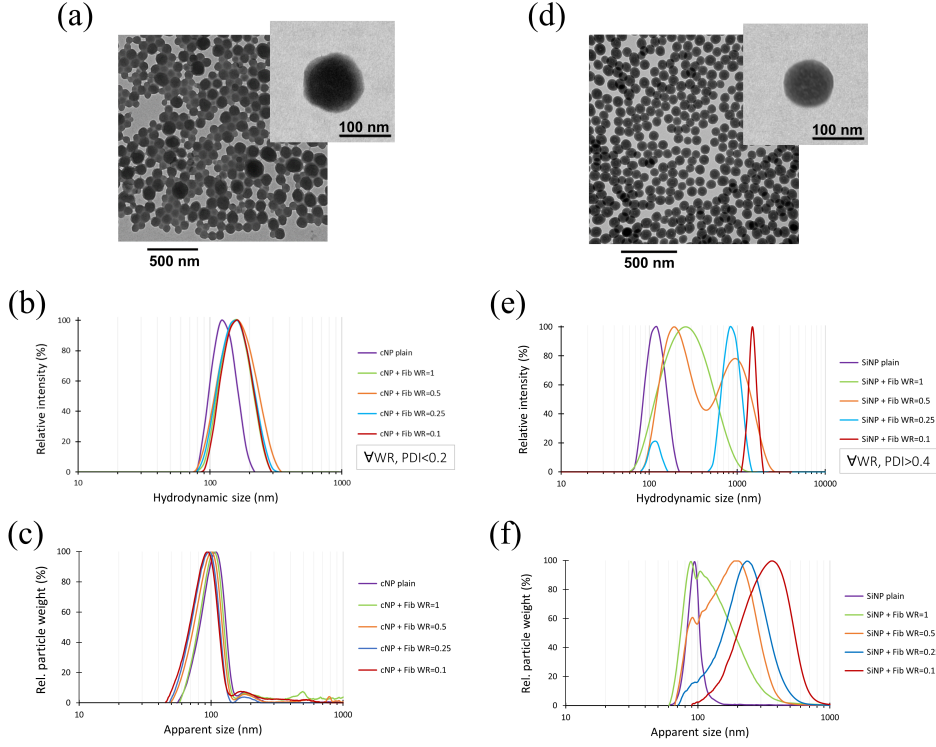


Fig. 2: Physicochemical characterization of the NPs and the Fib corona. (a) Transmission Electron Microscopy (TEM) image of CNPs with a nominal diameter of ~ 120 nm. After image processing, they were calculated to have a core diameter of (118.3 ± 40.8) nm. (b) DLS distribution for pristine ('plain') CNPs and in solution with Fib at WR between 0.1 and 1.0. In all cases, the polydispersity index (PDI) is less than 0.12. (c) DCS analysis for the corresponding cases. (d) TEM image of SiO₂NPs with a nominal diameter of 100 nm. Their calculated size of (95.4 ± 7.8) nm. (e) DLS of SiO₂NPs with PDI of 0.01, and (f) the corresponding DCS analysis.

image samples, TEM is able to provide high-resolution images and to characterize the size populations of NPs (Fig. 2a and d). Furthermore, by Dynamic Light Scattering (DLS), we characterize their polydispersity index (PDI). In DLS, a laser tracks the NPs' movement, due to Brownian diffusion, allowing the measurement of the auto-correlation function and diffusion coefficient, which in turn determine the particles' hydrodynamic size and PDI. We find that both CNPs and SiO₂NPs are monodisperse in aqueous solution and stable against aggregation, even though the former are hydrophobic and the latter are hydrophilic (Fig. 2a and d).

Next, we check whether the solutions of NPs covered by a corona of Fib are stable at room temperature. Previous experiments have shown that the addition of proteins in solution can induce NP aggregation [39], and that aggregation in simple media

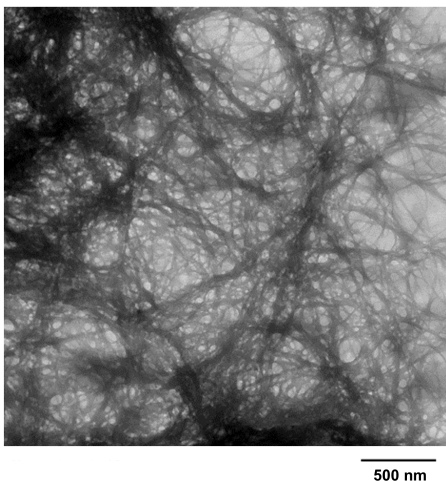


Fig. 3: TEM image of Fib aggregates under dried conditions obtained after heating the sample of human Fib at blood-like concentration (2 mg/ml) up to 88°C. The shape of the aggregate resembles the typical structure of fibrin fibers.

can occur at much lower protein concentrations than in complex media with many components [40].

Therefore, we analyze the stability of the NP-protein corona complexes against aggregation after incubation at different protein/NP weight ratios (WR from 0.1 to 1.0) using various techniques. By employing DLS and Differential Centrifugal Sedimentation (DCS), we do not observe aggregates for CNPs at the tested WRs (Fig.2 b and c). However, for the same range of WRs, aggregation systematically occurs with SiO₂NP (Fig.2 e and f).

Therefore, the difference in the NPs' chemistry likely impacts differently the protein adsorption and the aggregative propensity. Next, we set our experimental conditions to WR=1 and compare the cases of both CNP (colloidally stable) and SiO₂NP (colloidally unstable) with a free Fib solution at various temperatures.

First, we observe, by TEM characterization, that Fib at blood-like concentration agglomerates when the temperature reaches 88°C. The aggregates clearly resemble the structure of fibrin fibers [41] (Fig.3).

Next, our DLS analysis indicates that the hydrodynamic diameter of bulk Fib and Fib with silica NPs varies with temperature. In both cases, there is a heterogeneous PDI, with aggregation occurring at 52°C and above.

In contrast, the sample containing Fib and carbon NPs shows a homogeneous PDI at any temperature. However, at 52°C, it exhibits a shift in PDI that may be related to a gradual denaturation of Fib, which affects the solution's colloidal stability.

2.1.2 UV Resonance Raman Spectroscopy

UVRR spectroscopy is a powerful tool for detecting structural changes in organic biomolecules, such as proteins and peptides, without the need for any chemical label

[42]. Compared to spontaneous Raman spectroscopy using visible excitation sources, the UVRR technique offers undeniable advantages. The vibrational profiles of proteins typically result in a complex superposition of several signals, making analysis difficult. Thanks to the selective resonance enhancement achieved by appropriately tuning the excitation wavelength in the deep UV range (200-300 nm), UVRR spectra of proteins can be simplified, and the signals arising from selected chromophores or molecular portions of the molecule can be more easily disentangled [43–45]. In this regard, using Synchrotron Radiation (SR) as an excitation source for UVRR experiments provides the added advantage of fine-tuning the excitation wavelength to select the best working conditions for the system under investigation [46–48]. Additionally, the high sensitivity of the UVRR technique is crucial for investigating proteins in more diluted conditions compared to visible Raman spectroscopy while maintaining satisfactory quality in the spectra. This, in turn, provides the opportunity to simultaneously extract information from the UVRR spectra of proteins in aqueous solutions, both from the Raman signals attributed to the polypeptide solute and the water molecules in the hydration shell [47, 49].

We collect the UVRR spectra for Fib in PBS buffer, both in the presence and absence of NPs, using 226 nm as the excitation source (Fig. 4 a-d). This excitation energy falls within the absorption range of the aromatic rings of Tyrosine (Tyr) and Tryptophan (Trp) residues, resulting in UVRR spectra of Fib that are predominantly characterized by the vibrational signals of these aromatic amino acids [43, 50] (Fig. 4 a).

In the Raman spectrum of the Fib protein, we can identify several key resonance Raman features associated with the Trp vibrational modes, including signals at 1012 cm^{-1} (Trp W16), which are attributed to the symmetric benzene/pyrrole out-of-phase breathing, at 1340-1360 cm^{-1} (Trp W7), which is attributed to the Fermi resonance between N1-C8 stretching in the pyrrole ring and combination bands of out-of-plane bending, and at 1554 cm^{-1} (Trp W3), which relates to the C2-C3 stretching mode of the pyrrole ring [51]. In the same spectral range of 1000-1800 cm^{-1} , Tyr Raman bands are also detected, specifically the signals at 1176 cm^{-1} (Tyr Y9a), which are associated with in-plane C-H bending, and at 1616 cm^{-1} (Tyr 8a), which is due to the in-plane ring stretching of Tyr. Additionally, a signal at approximately 1770 cm^{-1} is observed in the UVRR spectrum of Fib, likely corresponding to a C=O stretching vibration.

Since the aromatic rings of Trp and Tyr can participate in hydrophobic, cation- π , and hydrogen-bond interactions with nearby residues or surrounding solvent molecules [51], the spectral feature parameters of the Raman bands associated with these residues provide valuable insights into their local environment. For instance, it has been reported that the vibrations of aromatic ring side chains in proteins can serve as sensitive markers for changes occurring in the tertiary structure of the proteins during unfolding and aggregation [22, 23, 52–54].

It is noteworthy that, in the spectral range of 1000-1800 cm^{-1} (Fig. 4 a), the Raman signal from the water solvent is practically negligible compared to the vibrational signals attributed to the Fib protein. Conversely, the high frequency range

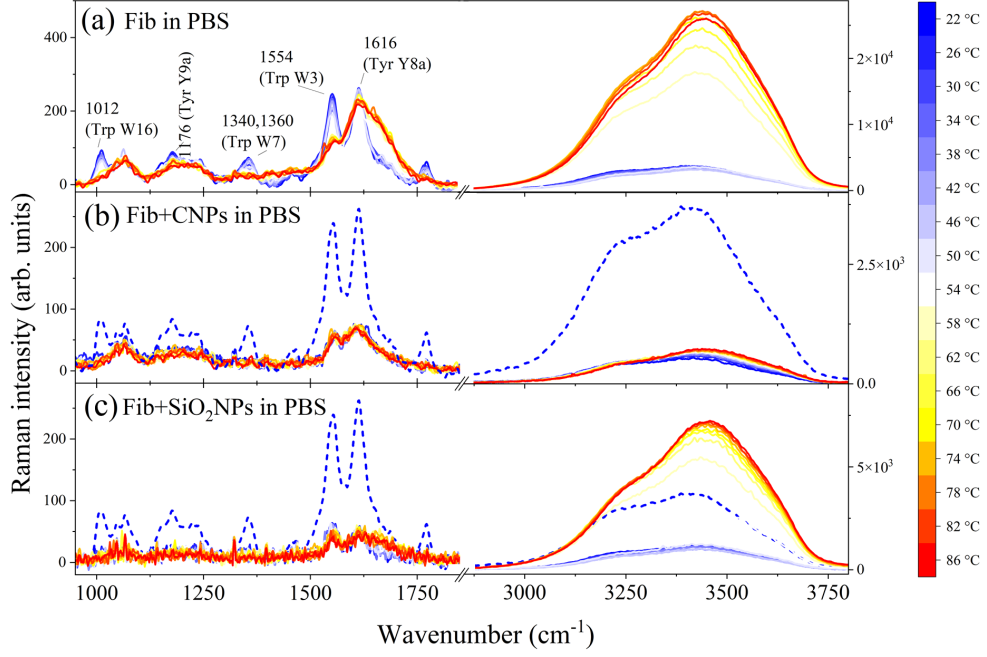


Fig. 4: 226 nm-excited UVR Raman spectra collected for Fib 2mg/ml in PBS pH 7.4 (a), Fib with CNPs (b) and Fib with SiO₂NPs (c) as a function of temperature, reported in the two spectral ranges 1000-1800 and 2800-3800 cm⁻¹. The main features in the spectrum of Fib are labelled in the panel (a). Temperature range and steps are indicated in the colour scale at the right. Dashed lines in panels (b) and (c) represent the spectra of Fib alone at the lowest temperature of 22°C.

between 2800 and 3800 cm⁻¹ in the UVR Raman spectrum of Fib is entirely dominated by the intense spectral distribution characteristic of the OH stretching profile of water.

Remarkable spectral variations can be detected as a function of temperature in both explored wavenumber regions for the protein Fib alone (Fig. 4a). In particular, the intensity of the Trp Raman signals W16, W7, and W3 significantly decreases starting from about 50-60°C. For the intense signal at ~ 1554 cm⁻¹ (Trp W3), the change is even more noticeable, as the peak almost disappears at high temperatures. Conversely, the signal assigned to the Tyr band at ~ 1616 cm⁻¹ appears stable as a function of temperature, while a new broad spectral contribution centered at about 1650 cm⁻¹ tends to rise with increasing temperature. At the same time, we observe a considerable increase in the total intensity of the OH stretching band of water when the temperature exceeds 50-60°C.

The spectra for Fib with CNPs (Fig. 4 b) clearly show that the Raman signal of the Fib protein, when introduced into an NP solution, decreases significantly, and some spectral features almost completely disappear or exhibit broadening. For example, this is evident from the comparison between the spectra of Fib alone and with

CNPs in the range of 1500-1800 cm^{-1} . This is partly related to the increase in UV absorption at 220-230 nm of the solution with CNPs compared to the pristine protein. In fact, self-absorption reduces the observed Raman intensities of Fib, which is clearly evident when looking at the total intensity of the OH stretching band of water (Fig. 4 b). More importantly, we can observe that by increasing the temperature, the Raman spectra of Fib with CNPs do not exhibit any remarkable change in both the explored wavenumber ranges, unlike the case of pristine protein. This experimental finding suggests that the presence of CNPs in solution tends to mitigate the effect of temperature on the structure of Fib.

For the spectra of Fib with SiO_2 NPs, we observe a T -dependence of the OH stretching band of water that resembles that of free Fib (Fig. 4 c). A more quantitative insight can be extracted from analyzing the temperature dependence of the intensities of some characteristic Raman signals (Fig. 5).

The integrated area of the OH stretching band for Fib alone (Fig. 5 a) exhibits a clear sigmoidal trend as a function of temperature, indicating a transition of the protein occurring at approximately 57°C. The sudden increase in this Raman signal above 50°C likely marks the unfolding and aggregation of the protein driven by the temperature rise. The sigmoidal trend suggests that protein denaturation begins at around 50°C and rapidly increases until 70°C, at which point the intensity of the OH band area stabilizes. Consequently, aggregates may be forming within this temperature range.

When CNPs are added to Fib's solution, the OH profile significantly decreases in intensity but retains its shape (Fig. 4 b). This may suggest that water is not able to penetrate the protein corona, likely due to protein unfolding on the surface of the NP. Additionally, the corresponding OH-band integrated area shows little to no dependence on T (Fig. 5 a). This finding suggests that the Fib corona is so strongly adsorbed that even with a significant increase in the energy of the solution due to heating, the proteins remain bound to the CNP. Furthermore, the analysis provides no evidence of aggregation.

When SiO_2 NPs are in solution with Fib, we observe that the OH-band integrated area is intermediate between the two previous cases, with a T -dependence that is weaker than for free Fib (Fig. 5 a). Furthermore, the increase in the area occurs at a temperature close to that of bulk Fib. This behavior suggests that Fib adsorbed onto SiO_2 NPs undergoes unfolding and aggregation similar to free Fib. Nevertheless, the analysis does not allow us to quantify the amount of unfolding and aggregation relative to the bulk case.

We also analyze the temperature dependence of the integrated area of some characteristic Raman signals in the fingerprint region 1000-1800 cm^{-1} assigned to Fib (Fig. 5 c-f). In particular, the unfolding and aggregation of proteins should alter the local packing of side chains and the solvent exposure of the residues, affecting the surrounding environment of Trp amino acids and the resonance Raman cross-section of the associated bands [50, 55, 56]. Therefore, by comparing their relative intensity for Fib in the absence and presence of NPs, we can qualitatively assess the effect of NPs on the T -dependence of the bands (Fig. 5 c-f).

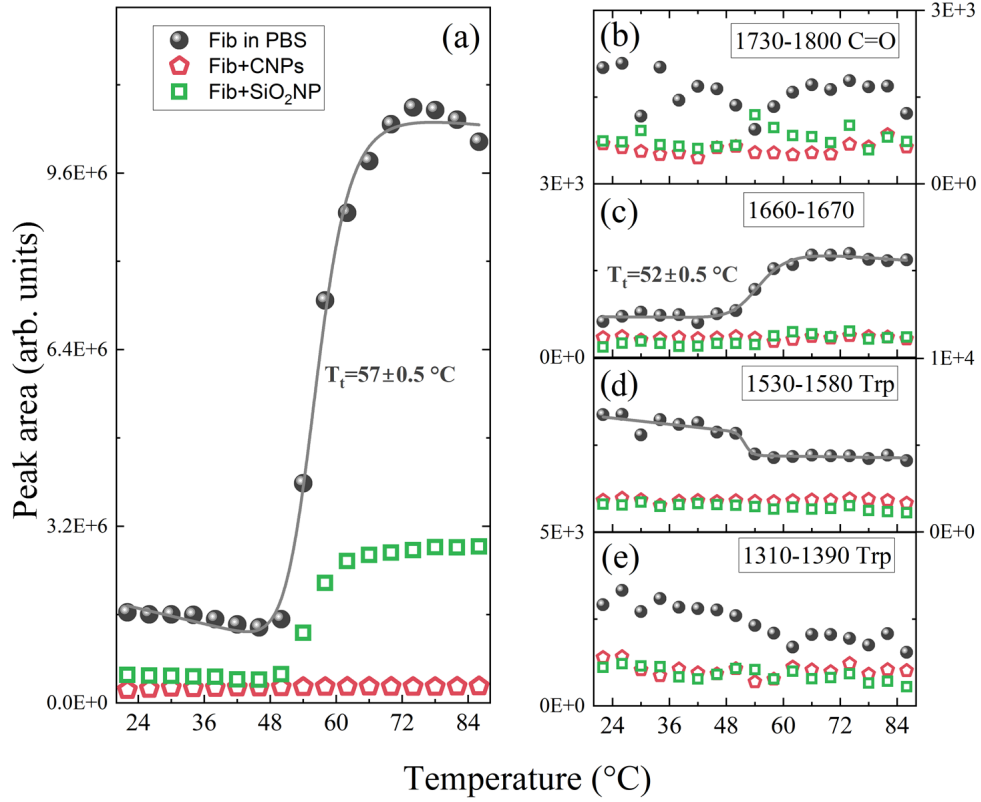


Fig. 5: Integrated area of the UVRR spectra in Fig. 4. (a) OH band area for Fib in PBS (black circles) and with CNPs (red pentagons), as well as SiO₂NPs (green squares). (b)-(e) Areas of the peaks in the frequency intervals reported in Table B1 for Fib in PBS and with CNPs and SiO₂NPs. In each panel, the frequency range is indicated as a label, and the symbols are the same as in panel (a). Where indicated, the experimental data have been fitted with a sigmoidal curve (full black lines).

Interestingly, for bulk Fib, we observe a rise in the spectral contribution between 1660-1670 cm⁻¹ starting from about 55°C (Fig. 5 c) and a decrease in the intensity of the Trp W3 band (Fig. 5 d) at about 52°C, while unclear features are evident for other peak areas. The two changes could represent two different events, such as unfolding and aggregation, or a single event in which both unfolding and aggregation occur at the same temperature, as debated in the literature. The experimental indeterminacy does not allow us to clearly contribute to the debate, although there are theoretical reasons to support the first interpretation [57].

When the solution includes the NPs, none of the band intensities exhibit a consistent tendency, hindering any clear interpretation (Fig. 5 b-e). Overall, these spectral

data reveal the difficulty of interpreting the experimental data and the necessity for a systematic method for their analysis.

2.1.3 Circular Dichroism and UV Absorption Spectroscopy

Circular dichroism (CD) is a widely used technique in biochemistry for studying the secondary structure of biomolecules. By examining the ellipticity $\theta\lambda$, which is proportional to the differential absorption of circularly polarized light, one can characterize how the chiral structures of proteins, such as alpha helices and beta barrels, change under various conditions. At the same time, the UV absorbance spectra serve as a complementary tool providing important information about protein stability, unfolding, and aggregation.

By combining CD/UV absorption spectroscopy with UVRr experiments, we aim to provide a comprehensive view of the structural changes in the Fib protein’s secondary and tertiary structures while overcoming the intrinsic limitations of each of the three techniques. Therefore, we collect UV and CD spectra as a function of temperature for the Fib protein, both alone and in the presence of NPs (Fig. 6 a-f).

We observe that at approximately 52°C in both the CD/UV absorbance spectra of free Fib and Fib with SiO₂NPs, there is a noticeable modification of the experimental profiles. Specifically, they indicate i) a decrease in UV absorption (Fig. 6 a and e), and ii) a change in Fib’s secondary structure (Fig. 6 b and f of the CD spectra). These changes correspond to an increase in the intensity of the water band in the Raman spectra for these two cases (Fig. 4 a and c).

On the other hand, the UV absorption of Fib with CNPs shows no T -dependence (Fig. 6 c), while the CD spectra, which are noisy due to CNP’s absorption, exhibit a T -dependence that is weaker than those observed for free Fib and Fib with SiO₂NPs (Fig. 6 d). These data are only partially consistent with the corresponding results from UVRr spectra, displaying a very weak dependence of the spectra on temperature (Fig. 4 b).

These trends can be emphasized by selecting the signals at a specific wavelength and analyzing them as a function of temperature. For UV absorption, we select the signal at 225 nm (Fig. 6 g), while for CD, we choose the ellipticity $\theta\lambda$ at 222 nm (Fig. 6 h). For both quantities, we observe some similarities between Fib in PBS and Fib with SiO₂NPs, while no or weak T -dependence for Fib with CNPs.

Therefore, as with the UVRr spectra, while we observe differences and similarities among the three cases, no quantitative results can be systematically extracted from these data. To achieve an analysis of the spectroscopic data that quantitatively evaluates how far the NP-adsorbed proteins are from their native state, we have developed a method based on ML approach for the combined spectra.

2.2 Machine Learning Automate Workflow for High-dimensional Composite Spectra

To prepare the acquired spectral data for treatment using our proposed ML workflow, we first apply data curation through baseline corrections, followed by appropriate spectral truncations, removing the silent regions from the UVRr spectra and the noisy

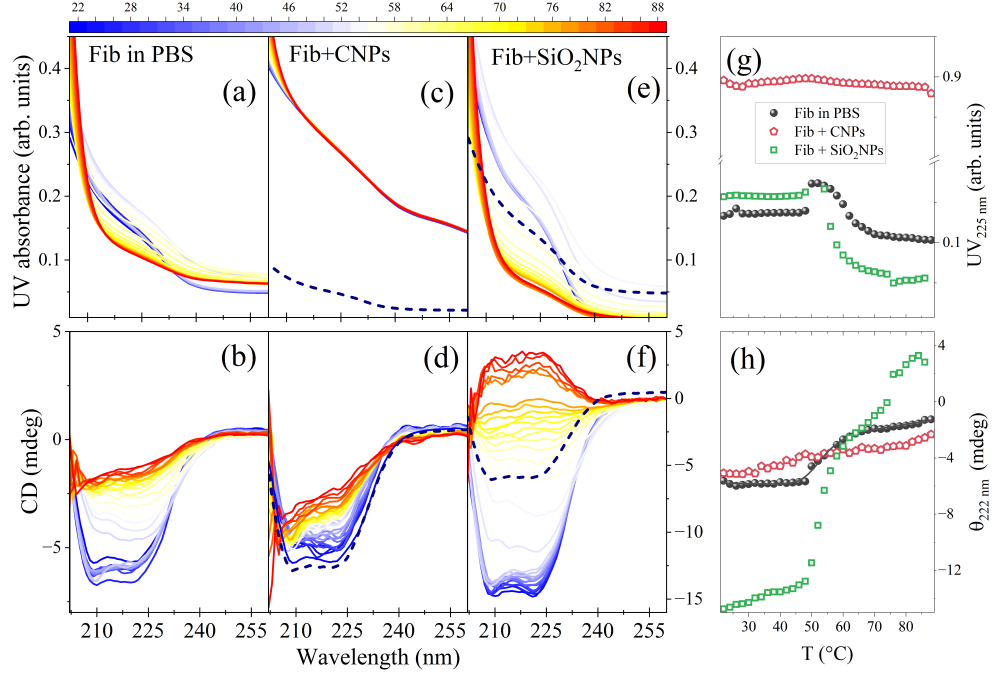


Fig. 6: Temperature-dependent UV absorption and CD spectra collected for Fib 2 mg/ml under various conditions. In all panels, the temperature ranges between 22 and 88°C. Upper panels a), c), and e) are the UV absorption spectra for Fib in PBS pH 7.4, Fib with CNPs, and Fib with SiO₂NPs, respectively. Lower panels b), d), and f) are the corresponding CD spectra. Curves with different colors correspond to different temperatures as indicated by the upper color bar. Dashed lines in panels c)-f) represent the spectra of panels a) and b) at the lowest temperature, provided here as a reference. Panels g) and h) display the UV absorbance at 225 nm, and the ellipticity θ_{222} , measured in millidegrees (mdeg), at 222 nm, respectively, for the three cases: free Fib in PBS (black circles), Fib with CNPs (red pentagons), and Fib with SiO₂NPs (green squares).

regions from the CD and UV absorption spectra (see Section B.4 for details). The preprocessed spectra for each system (free Fib, Fib with carbon NPs, Fib with silica NPs) are then combined into a higher-dimensional vector that captures all significant chemical information at each temperature.

Next, we implement data standardization, which is typically necessary for PCA and t-SNE analysis. Specifically, this procedure accounts for the fact that the data at hand are measured in different units [31, 35, 58].

Finally, we apply the ML model, which includes (i) metric analysis, (ii) clustering, manifold reduction, and (iii) the subsequent elaboration of the outputs. Different tools, such as Euclidean and Manhattan distances, along with PCA, are routinely used to analyze high-dimensional and spectral data. For example, the distances can

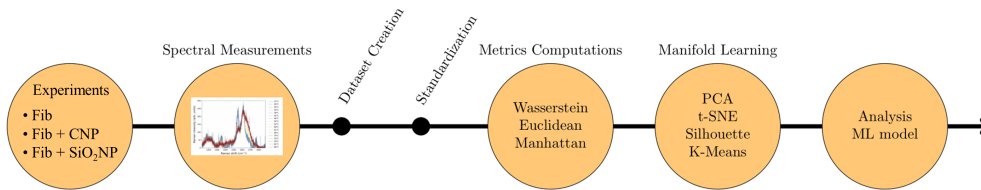


Fig. 7: Work pipeline including the automated ML workflow. The first two steps (circles) represent the experiment execution and output spectra. In the case considered here, we prepare solutions containing Fib—either alone or in combination with CNPs or SiO₂NPs—and perform spectral measurements of these systems at various temperatures. Next, data curation and standardization of the experimental outputs are applied. Then, preprocessed data are analyzed using metrics computation and manifold learning via unsupervised ML tools, enabling quantitative and qualitative analysis.

measure the similarity between pairs of spectra to quantify the structural changes of proteins, while PCA can visualize the patterns of the original data spectra in a two-dimensional space. However, these traditional tools encounter issues due to the variety and high dimensionality of the data at hand. For this reason, we replace them with the Wasserstein distance and t-SNE, respectively, as discussed in the next section. Our entire work pipeline, starting from the experiments and concluding with the ML analysis, is illustrated in Fig. 7.

3 ML model

The key idea behind our ML model is to use a physics-informed metric to identify and quantify potential protein conformational changes in our solutions, caused by increasing the temperature. However, since the spectral data is high-dimensional, it is also essential to visualize emerging patterns and assess their consistency with the metric analysis. With this in mind, we select the best state-of-the-art tools for this problem: the Wasserstein distance and t-SNE.

The Wasserstein (or Earth Mover’s) distance, defined in Eq. B2, measures the distance between two probability distributions. It circumvents the challenges of the *curse of dimensionality* by calculating the minimum transport-based cost required to transform one distribution into another, primarily comparing spectra based on their shapes rather than directly relying on spectral intensities [59]. In contrast, similarity measures such as Euclidean and Manhattan distances (defined in Table B2), which are commonly used, focus solely on intensity differences. As a result, they are unreliable when handling high-dimensional data.

The t-SNE is a nonlinear dimensionality reduction technique that converts high-dimensional data into a probability distribution reflecting the similarities among data

points. It is specifically designed to address the crowding problem, which refers to the risk of losing local structure and compressing distances when high-dimensional data is mapped to a lower-dimensional space. The t-SNE mitigates the crowding problem because the heavy tails of the Student-t distribution in the low-dimensional space allow for better separation of points that are moderately distant. When applied to complex, high-dimensional data where local relationships are crucial, t-SNE outperforms the faster PCA, which cannot effectively handle data from different sources due to its reliance on variance maximization. This maximization can be significantly influenced by outliers, resulting in misleading results.

In our metric computations, we consider as reference spectra those taken at $T_0 = 22^\circ\text{C}$, which is the lowest temperature of our measurements. At T_0 , Fib is in its native state. As a result, we compute the similarity distance between the composite spectrum at T_0 and the other spectra at temperatures T , separated by $\Delta T = 4^\circ\text{C}$. Accordingly, the Wasserstein distance quantifies the increase of the protein’s structural disorder with temperature. To emphasize the change, we normalize the Wasserstein distance with the two values at the two extreme temperatures for the free Fib case (Fig. 8).

We find that the disorder content of the protein increases monotonically with temperature for all systems. In particular, the normalized disorder content for the free Fib and the Fib with silica NPs depends on temperature in a similar way. In both cases, around $(52 \pm 2)^\circ\text{C}$, the normalized Wasserstein distance experiences a significant change, while outside that range, the increase is approximately linear.

Comparing this analysis with the original experimental spectra and our knowledge of the temperature range for unfolding the free Fib in solution, we conclude that the characteristic temperature $(52 \pm 2)^\circ\text{C}$ indicates the unfolding transition for both free Fib and the Fib with silica NPs. Therefore, the adsorption of Fib onto SiO_2 NPs does not affect the Fib unfolding temperature.

However, while the free Fib attains the reference value of one at $T = 86^\circ\text{C}$, the protein with the silica NP only reaches a value of 0.9 at the same T . Hence, the silica surface partially limits the unfolding of Fib.

In contrast, the effect of the carbon interface is significantly different. In this case, the increase in the normalized Wasserstein distance is approximately linear across the entire range of explored temperatures, with no indication of a rapid structural change as in a folding-unfolding transition. Furthermore, the distance at 86°C only reaches a value of 0.5. Conventionally, a value of 0.5 for a folding-unfolding structural parameter is the limit between the two states. Furthermore, for the other two cases, the larger structural change occurs when the Wasserstein parameter is approximately 0.5.

Therefore, the impact of the NP surface is substantial, inducing only a gradual structural change. This analysis enables us to better interpret the original spectra, clarifying that the structural disorder induced by the increase in temperature in this case does not resemble the standard unfolding that occurs for the free protein.

These observations regarding the differences in the Wasserstein distances of Fib proteins interacting with hydrophilic silica NPs and hydrophobic carbon NPs indicate that the two interfaces impact Fib’s structure in fundamentally different ways. Furthermore, recalling that we normalize the Wasserstein distance relative to the minimum and maximum disorder in the free Fib case, Fig. 8 provides information about

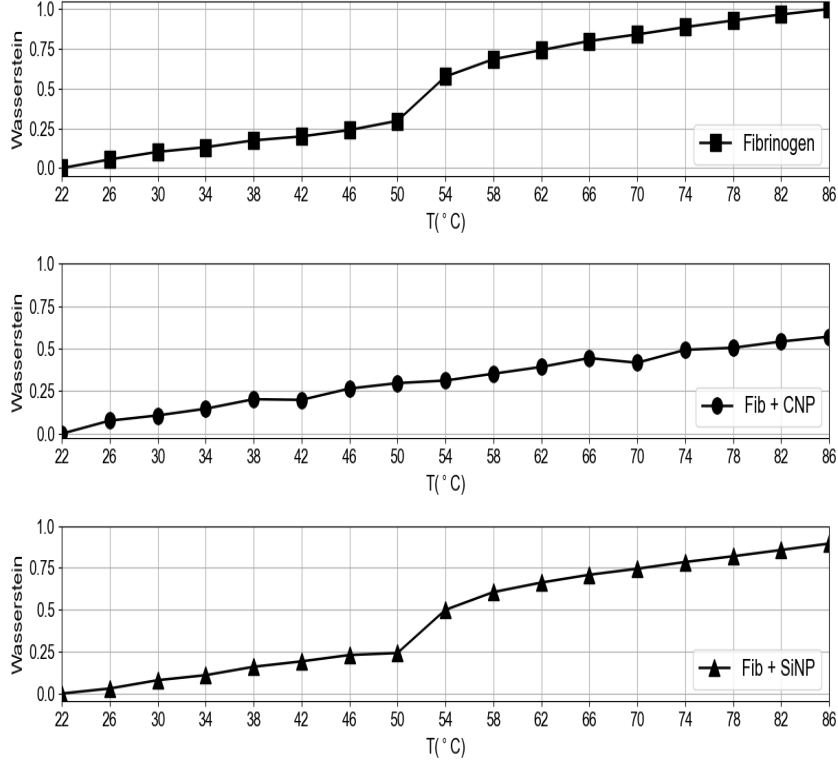


Fig. 8: Normalized Wasserstein distance computed for composite spectra of free Fib and Fib with NPs. Upper panel: free Fib (squares). Central panel: Fib with CNPs (circles). Lowe panel: Fib with SiO₂NP (triangles). In each case, the quantity is normalized with respect to the values at 22°C and 86°C for the free case, corresponding to Fib in its native (folded) or disordered (unfolded) state. Therefore, it quantifies the relative distance of the spectra (structural disorder) from the reference spectrum of a free Fib protein in its native state at 22°C.

the absolute value of disorder as a function of T in each case. In particular, Fib on silica NPs unfolds approximately 90% of the free case, while Fib on carbon NPs is about 50% folded at the same T .

It is worth noting that using Euclidean and Manhattan distances would result in a different erroneous scenario, where several substantial changes, even at the lowest temperatures, appear across the temperature range. This is discussed in Section 2 (Figs. S2a, S2b) of ESI.

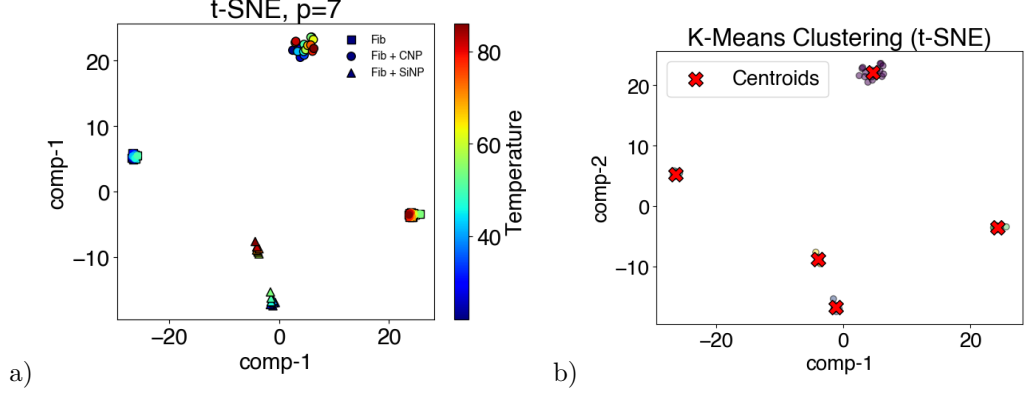


Fig. 9: t-SNE analysis of composite spectra. a) Two-dimensional embedding from t-SNE with cosine similarity of composite spectra of free Fib (squares), Fib with CNPs (circles), and Fib with SiO₂NPs (triangles), each corresponding to a given temperature. Temperatures are indicated in the color bar, with $\Delta T = 4^\circ\text{C}$ starting from $T = 22^\circ\text{C}$. We used $\mathcal{P} = 7$ and PCA initialization for t-SNE computations. b) Same as in panel a), with centroids (red cross marks) computed using the K-means clustering algorithm, assuming the optimal number of clusters $n_{\text{op}} = 5$ as input. In this case, the average silhouette score is ≈ 0.94 .

To better interpret the absolute amount of disorder the Fib acquires with temperature increase in each case, we apply t-SNE to the data under scrutiny. This manifold learning algorithm models similarities between composite spectra in the original high-dimensional space using a Gaussian distribution and maps it into a Student-t distribution in the low-dimensional space [29]. It then minimizes the Kullback–Leibler (KL) divergence between the probability distribution of the original high-dimensional data and the low-dimensional space, which in our case is two, visualizing a corresponding two-dimensional embedding [29]. The KL divergence is a non-symmetric measure of similarity between two distributions, which, when minimized, preserves the local structure of the data. Hence, if two points are close in high-dimensional space, a minimum KL divergence keeps them close in the low-dimensional space as well.

To compute t-SNE, an input parameter called the perplexity \mathcal{P} is required. The perplexity roughly corresponds to the effective number of neighbors in the high-dimensional space for each point considered when calculating similarities. In cases where several thousand data sets are available, the suggested default values for \mathcal{P} are between 30 and 50 [30]. However, in our case, due to the small size of each dataset with only 17 temperatures, we propose to automatically find the optimal value of \mathcal{P} through a grid search based on K-means clustering, a popular unsupervised ML algorithm used for clustering data, and the average silhouette score, which gives an overall measure of how appropriately the data has been clustered, as discussed in Section 4 of ESI [58, 60]. According to our procedure, the perplexity is set to 7, consistent with the small size of the datasets. Other parameters are set to their default values for t-SNE optimization [30].

To calculate the embedding, we compute t-SNE using cosine similarity (Eq. B1), as it is expected to make t-SNE less susceptible to the high dimensionality of the spectral data. We identify five distinct clusters (Figure 9a).

All data corresponding to free Fib (squares) and Fib with SiO₂NPs (triangles) are divided into two clusters, each characterized by distinct temperature ranges: $T \leq 50^\circ\text{C}$ and $T \geq 54^\circ\text{C}$. The emergence of two clusters for free Fib and Fib with SiO₂NPs indicates a significant conformational change around $(52 \pm 2)^\circ\text{C}$, consistent with our interpretation of the normalized Wasserstein metrics as a measure of protein disorder, which signifies the folding-unfolding transition of Fib as the temperature increases.

The remaining data for Fib with CNPs (circles) are grouped into a single cluster. This indicates that, at all analyzed temperatures, no significant structural change occurs, further supporting our rationale that a normalized Wasserstein distance with a value of approximately 0.5 corresponds to a protein that is around 50% folded.

The calculation of centroids based on the K-means algorithm, with the number of clusters set to 5, confirms that the data instances are well clustered. The clustering pattern has an average silhouette score of approximately 0.94, indicating strong clustering [58] (Fig. 9 b).

This analysis demonstrates that, for normalized Wasserstein distance up to 0.5, the change in the Fib structure is limited, as with CNPs. Above the 0.5 value, the Wasserstein parameter marks an unfolded state, as with free Fib and Fib with silica NPs.

Although not quantitative, the t-SNE analysis qualitatively confirms that the structural change for Fib with SiO₂NPs is less significant than in the free Fib case, even though the Fib unfolds at the same temperature in both scenarios. In contrast, it highlights the gradual increase of disorder without unfolding for Fib adsorbed on the hydrophobic carbon NPs up to 86°C .

We emphasize that if PCA is used instead of t-SNE, the resulting two-dimensional projection would suggest the presence of five or more clusters. Furthermore, the calculation of the centroids would be less clear, making it more difficult to quantitatively evaluate the absolute amount of structural disorder in the three cases. This is because PCA identifies some data points as outliers, as discussed in Section 3 of the ESI, due to its difficulty in handling data originating from very different sources.

Finally, we note that a similar embedding is obtained when computing t-SNE with the Euclidean norm/distance and $\mathcal{P} = 7$, as discussed in Section 4 of the ESI. In this case, the clustering quality decreases, with the average silhouette score dropping to approximately 0.91. Nevertheless, five well-defined clusters still emerge, reinforcing the idea that t-SNE is not significantly affected by the data’s high dimensionality.

4 Conclusion

We developed a method that leverages ML to interpret spectral data from multiple experimental techniques, measuring the structural properties of proteins. This approach optimizes the combined information and systematically evaluates the relative and absolute structural disorder of proteins as a function of varying external conditions.

We apply the method to the combined data from UVRR, CD, UV, and DLS measurements. These techniques provide complementary insights into the protein’s secondary and tertiary structural changes, aggregation behavior, and overall colloidal stability.

As a relevant case study, we consider the debated effect of NP surface chemistry on the structural changes of proteins adsorbed within the corona at varying temperatures. To achieve this goal, we consider fibrinogen at blood concentrations when interacting with hydrophobic carbon or hydrophilic silicon dioxide nanoparticles. Our findings demonstrate that the NP chemistry has a significant impact on the stability of Fib as a function of temperature, with striking differences between the hydrophilic and hydrophobic cases.

Specifically, our ML method demonstrates that silica NPs reduce the Fib’s structural changes at increasing temperatures by 10% compared to the free Fib case. Furthermore, our approach identifies the adsorbed Fib unfolding transition temperature at $(52 \pm 2)^{\circ}\text{C}$, which coincides with the temperature at which free Fib unfolds. Above and below this characteristic temperature, the relative disorder of Fib adsorbed on the silica NPs follows the same linear trend as the free Fib. At high T , this trend is associated with an aggregation process. Therefore, the interaction with the hydrophilic surface moderates the protein unfolding but does not qualitatively change its aggregation compared to the free protein case. These experimental results confirm recent theoretical predictions based on simple modeling of hydrated proteins adsorbing onto a hydrophilic interface [18].

The ML method reveals that the results are drastically different when Fib interacts with hydrophobic carbon NPs. Our analysis shows that the proteins interacting with CNPs do not undergo an unfolding transition at any of the explored temperatures between 22 and 86°C , contrary to the bulk and silica NP cases. The Fib structure, on the other hand, reaches a mildly disordered state, without undergoing an unfolding transition, even at the highest T explored when adsorbed onto the hydrophobic CNP surface. This effect, in turn, reduces the aggregation phenomenon with temperature. Therefore, the ML method enables us to clearly confirm, for the first time, the stabilization effect of a hydrophobic surface against protein conformational changes and aggregation, as predicted by recent theoretical modeling [17].

Overall, our ML workflow presents a unique perspective on the potential applications of protein corona by using NPs with specific properties. This is particularly significant given the increasing use of NPs in various medical contexts, such as drug delivery and imaging. These findings suggest that engineering NP surface properties can lead to novel methods for modulating protein stability and hold substantial promise for therapeutic and diagnostic applications. For example, adjusting the NPs’ surface to be more hydrophobic or hydrophilic could facilitate differential control over protein aggregation, thereby enhancing stability under physiological conditions.

In conclusion, our novel application of ML algorithms provides a unique analytical perspective on characterizing protein structural changes upon adsorption to nanomaterials. Future applications of these methods could explore broader environmental conditions, such as pH, ionic strength, or the presence of other biomolecules,

in more complex biological milieus, thereby further advancing the understanding of protein-NP interactions and their practical implications.

Acknowledgments

All authors acknowledge Elettra Sincrotrone Trieste for providing access to its synchrotron radiation facilities and for financial support under the IUS internal project. A.M.-S. and M.P.M. gratefully acknowledge the financial support through the H2020 SUNSHINE grant no. 952924. G.F. and G.M. acknowledge the support by MCIN/AEI/ 10.13039/ 501100011033, the European Commission “ERDF A way of making Europe” grant number PID2021-124297NB-C31, and the support by ICREA Foundation (ICREA Academia prize). G.F. also acknowledges the support from the Ministry of Universities 2023-2024 Mobility Subprogram within the Talent and its Employability Promotion State Program (PEICTI 2021-2023), the Visitor Program of the Max Planck Institute for the Physics of Complex Systems for supporting a visit started in November 2022, the COST Action CA22143 EuMINe. G.M. would like to thank Jozsef Kardos for his help in using the BeStSel software. All authors thank Oriol Miró for testing the code.

Authors’ contributions

A.M-S. performed the experimental measurements and supported the design and implementation of the analysis. G.M. designed and implemented the Machine Learning pipeline/protocol. F.D. and B.R. provided support for the spectroscopic measurements. B.R. coordinated the activity at Elettra Sincrotrone. I.F. provided the nanoparticles. A.M.-S. and G.M. wrote the first version of the manuscript. A.M.-S., G.M., and B.R. processed the data and prepared the figures. A.M.-S., G.M., B.R., M.M., and G.F. discussed the analysis, the strategies for their elaboration, and the interpretation of the results. G.M., A.M-S. and G.F. discussed the design of the computational method and the strategies for its implementation. G.M. prepared the support webpage repository for the open-source codes. B.R., M.M., and G.F. prepared revised versions of the manuscript. A.M-S. wrote the final draft. All the authors discussed and contributed to the final version of the manuscript. M.M. and G.F. acquired funds, designed the study, and coordinated the experimental and theoretical activities.

Conflict of interest

There are no conflicts to declare.

Additional information

Supplementary information

The online version contains supplementary material available upon request.

Availability of data and materials

The spectroscopic data used in this paper are available upon request.

Code availability

The codes used in the present paper are available upon request.

Appendix A Materials

SiO₂NPs of 0.1 μ m (stock concentration of 50 mg/mL) were provided by Kisker Biotech GmbH (Germany). CNPs were synthesized in the lab. Phosphate buffer saline (PBS) tablets, Eppendorf LoBind microcentrifuge tubes, Fibrinogen from human plasma (F3879) and D-(+)-Sucrose (99.9%) were purchased from Sigma-Aldrich (Ireland). One PBS tablet was dissolved in 200 mL of ultrapure water to obtain a 0.01 M phosphate buffer, 0.0027 M potassium chloride and 0.137 M sodium chloride solution (pH 7.4 at 25°C). TEM grids of Formvar / Silicon monoxide 200 mesh with copper approximate grid hole size 97 μ m were purchased from Ted Pella (USA).

Appendix B Methods

B.1 Experimental details

B.1.1 Carbon nanoparticle synthesis

Carbon nanoparticles of 100 nm nominal diameter were synthesised using the method developed by Kokalari et al. [61] They were produced by carbonization of glucose in water, consisting mainly of amorphous carbon with graphitic residues incorporated in the amorphous matrix. Compared to other carbon nanomaterials, they have the advantage of being produced by a synthesis that does not involve toxic solvents, with a high yield and, moreover, with a great control of the dimensions having a low variability from lot to lot. They also have a functionalized surface that makes them stable and negatively charged in water thanks to the acidic carboxylic groups exposed on the surface.

B.1.2 Nanoparticle characterization

Dynamic Light Scattering (DLS) measurements were performed using Zetasizer Nano ZS (Malvern). The sample cuvettes were equilibrated at 25°C for 90 s. For each measurement, the number of run and duration were automatically determined and repeated three times. Data analysis has been performed according to standard procedures and interpreted through a cumulant expansion of the field autocorrelation function to the second order.

Differential Centrifugal Sedimentation (DCS) experiments were performed with a CPS Disc Centrifuge DC24000, using the standard sucrose gradient 8-24% (Analytik Ltd.). The densities were set as 1.4 and 2 g/cm³ for CNP and SiO₂NP, respectively. A 544nm PVC calibration standard was used for each sample measurement. The time taken for spherical particles with homogeneous density to travel from the center of

the disk to the detector can be directly related to the apparent particle size, assuming spherical shape.

Transmission electron microscopy (TEM) images were obtained with a JEOL JEM-1400PLUS transmission electron microscope operating at an acceleration voltage of 120 kV. The statistical analysis was carried out using ImageJ and average size and standard deviation was measured on 103 NPs.

B.1.3 Protein Corona obtention

1ml of the synthesized CNPs with a concentration of 2mg/ml were introduced to low protein binding 1.5ml microtubes. 4mg of Fib were weighted using a microbalance and diluted from the stock in the NP solution. Then, a total volume of 500 μ l from the solution was transferred to a 1mm cell to perform the UVRR. For the DLS, the in-situ corona was diluted ten times to get an optimal attenuation after incubation at 37 °C for 10min under continuous agitation at 300 rpm. Therefore, 250 μ L of NP from the initial solution and 250 μ L of a 4mg/ml Fib solution in PBS were mixed, in order to a 0.5 mg/ml solution of both protein and NP (weight ratio 1). Then, the solution was incubated at 37 °C for 30min under continuous agitation at 300 rpm. After incubation, the NP corona complex was pelleted from excess proteins by centrifugation at 12.000g, 4°C for 15 min. The supernatant was discarded and the pellet was then resuspended in 500 μ L PBS and centrifuged again. The washing procedure removes unbound and loosely bound proteins from the NPs. The NP-corona complexes are obtained after repeating the washing procedure three times.

B.2 UV Resonant Raman measurements

UVRR spectra were collected by using the synchrotron-based UVRR set-up available at the BL10.2-IUVS beamline of Elettra Sincrotrone Trieste (Italy). [62] The excitation wavelength at 226 nm was obtained by setting the energy of the emission of the Synchrotron Radiation (SR) light by regulating the undulator gap aperture. The incoming SR light was further monochromatized through a Czerny-Turner monochromator (750 nm focal length Acton SP2750, Princeton Instruments, Acton, MA, USA) equipped with a holographic grating with 3600 grooves/mm. The Raman signal of the protein solutions was collected in back-scattered geometry and analyzed via a single-pass Czerny-Turner spectrometer (Trivista 557, Princeton Instruments, 750 mm of focal length) equipped with a holographic grating at 1800 g/mm. A thermoelectric cooled CCD camera optimized for the UV range was used to detect the signal at the output of the spectrometer. The resolution was set at about 1.6 cm^{-1} /pixel. Cyclohexane (spectroscopic grade, Sigma Aldrich) was used for the calibration of the wavenumber scale. The final radiation power on the samples was about 20 μ W. To avoid photodegradation during the measurements, the samples were continuously oscillated with 1 Hz frequency and a path length of 1 mm. For the collection of the temperature-dependent measurements (in the temperature range 295-359 K with step of 4 K) on protein solutions a sample holder equipped with a thermal bath coupled to a resistive heating system was used to control the temperature with a stability of \pm

0.1 K. The solution of protein with and without NP were measured at concentration of 2 mg/ml (the same weight/molar concentration was kept for protein and NP).

B.3 Circular dichroism and UV absorption measurements

CD and UV absorption spectra were recorded using a Jasco J-810 polarimeter equipped with a plug-n-play single-cell Peltier with temperature control. We measured the samples of protein solution without and with NP in PBS buffer 0.01 M pH=7.4 at concentration of 0.5 and 0.25 mg/ml, respectively. The spectra were collected in the temperature range 22-87 °C with steps of 2 °C. The same weight/mol concentration of NP and protein was kept. All the solutions were freshly prepared in a rectangular quartz cell with a 1 mm path length. Each CD and UV spectrum was collected in the range from 260 to 190 nm with an increment of 1 nm, a 20 nm/min scan rate, and a 1 nm bandpass. Measurements were performed under a constant nitrogen flow and the spectra were averaged from 4 scans. For each set of temperature-dependent measurements, the spectra of the solvent (PBS and solution of NP in PBS at concentration of 0.25 mg/ml) were subtracted from the corresponding samples ones.

B.4 Data Curation

The data obtained through different spectral techniques form a dataset containing UVRR, CD, and UV absorption spectra of Fib alone or in conjunction with CNP or SiO₂NP for each temperature T, ranging from 22 to 86 °C, taken at temperature intervals of $\Delta T = 4$ °C. This results in an overall number of 17 spectra for each type of spectroscopic method. The UVRR spectra encompass silent regions where there is no useful information. Through spectral truncation [63], these regions are removed, retaining the following five intervals (see Section 2.1.2), which are reported in Table B1.

Interval (cm ⁻¹)	n_c	Signature
2800 – 3800	632	OH Band
1730 – 1800	41	C=O
1660 – 1670	6	Peak
1530 – 1580	29	Trp
1310 – 1390	45	Trp

Table B1: The UVRR spectral intervals in cm⁻¹ unit under scrutiny together with the corresponding significant feature of interest and number of spectral components (or spectral intensities) n_c . Note that the interval 1660 – 1670 cm⁻¹ corresponds to a region of bulk Fib where a peak disappears altogether.

In CD and UV absorption spectra, we exclude spectral intervals below 210 nm because their signals are saturated due to the strong absorption of the buffer in such a wavenumber region. Consequently, after this spectral truncation, the available data ranges from 210 to 260 nm, corresponding to a total number of spectral components (or spectral intensities) denoted as $n_c = 51$.

It is worth noting that the spectral truncation applied to CD spectra should address the challenges encountered when attempting to predict the secondary structure of Fib in the presence of CNP using the full spectral range (i.e., 190-260 nm) with the *BeStSel* software [25, 64]. Specifically, while the software reasonably predicts zero content of α -helix structure of bulk Fib at high temperatures, it fails to do so for the protein’s spectra in the presence of CNP (see Figure S1 in Supplementary Materials). In this regard, we also found that when regression through Gaussian processes (GPs) [65, 66] is applied to spectra of Fib + CNP, the performance deteriorates, indicating an increase of noise in the spectral data. This analysis is reported in Supporting Information.

Finally, we merge the spectra for each system type—bulk Fib, Fib with CNPs, and Fib with SiO₂NP—to create new composite spectra that contain significant spectral information as discussed above. These new spectra are formed by concatenating the UVR-R intensities of five spectral intervals (as reported in Table B1), starting from the bottom in ascending order, along with the respective UV intensities, and then appending the CD intensities. As a result, the composite spectra under investigation consist of 856 dimensions.

B.5 Definitions of Metrics

Denoting two spectra by the sets $\{(\nu_1, I_1), (\nu_2, I_2), \dots, (\nu_N, I_N)\}$, $\{(\nu_1, Z_1), (\nu_2, Z_2), \dots, (\nu_N, Z_N)\}$, where ν_i is the wavenumber and I_i, Z_i the corresponding intensities, their similarity (or equivalently their dissimilarity) will be measured by computing a suitable distance between the vectors: $\mathbf{I} = (I_1, I_2, \dots, I_N)$, $\mathbf{Z} = (Z_1, Z_2, \dots, Z_N)$, where N corresponds to the number of the spectral observations. In Table B2 we report the mathematical formulae of Euclidean and Manhattan metrics, commonly used for assessing the similarity between the spectra.

Table B2: Formulae of Euclidean and Manhattan metrics

Similarity metric	Formula
Euclidean	$\left(\sum_{i=1}^N (I_i - Z_i)^2\right)^{1/2}$
Manhattan	$\sum_{i=1}^N I_i - Z_i $

For the sake of completeness, we also report the formula for the cosine similarity d_{\cos} between two spectral intensity vectors \mathbb{I} and \mathbb{Z} . It proves beneficial for the computations with t-SNE. The cosine similarity reads [25]:

$$d_{\cos}(\mathbf{I}, \mathbf{Z}) = 1 - \frac{\mathbf{I} \cdot \mathbf{Z}}{\|\mathbf{I}\|_2 \|\mathbf{Z}\|_2}, \quad (\text{B1})$$

where $\|\cdot\|_2$ is the Euclidean norm.

Next, the family of Wasserstein distances W_p ($p = 1, \dots$) arises from the Kantorovich formulation of Monge’s mass transport problem [67–69]. The optimal transport distance W_p is defined between probability distributions for a given metric. Thus, given two probability distributions $f(\mathbf{x})$ and $g(\mathbf{y})$ ($\mathbf{x}, \mathbf{y} \in \mathbb{R}^n$), the Wasserstein distance yields the minimum work required to transform one distribution to the other. In the present work, we shall consider the one form of Wasserstein distance $W_1(f, g)$, that is, $p = 1$, is defined as the minimum of the following expectation value [70]:

$$W_1(f, g) = \min_{\gamma \in \Gamma} E_{\gamma}[d(\mathbf{x}, \mathbf{y})], \quad (\text{B2})$$

where d denotes the Euclidean distance (see Table B2), and Γ is the family of joint probability distributions $\gamma(\mathbf{x}, \mathbf{y})$ whose marginal distributions are $f(\mathbf{x})$ and $g(\mathbf{y})$. This metric is implemented in Python library SciPy [71].

Applying the Wasserstein distance to spectra requires interpreting them as discrete probability distributions (or, equivalently, discrete probability measures) [27]. As a result, the spectral intensities must be nonnegative numbers and normalized to unity. These requirements can be easily met by translating all the multicomponent spectra of a given system and dividing the respective intensities by their total sum. Finally, we note that for computations using the Wasserstein distance, the data do not need to be standardized.

References

- [1] Soliman, M.G., Martinez-Serra, A., Antonello, G., Dobricic, M., Wilkins, T., Serchi, T., Fenoglio, I., Monopoli, M.P.: Understanding the role of biomolecular coronas in human exposure to nanomaterials. *Environmental Science: Nano* **11**, 4421–4448 (2024)
- [2] Waheed, S., Li, Z., Zhang, F., Chiarini, A., Armato, U., Wu, J.: Engineering nano-drug biointerface to overcome biological barriers toward precision drug delivery. *Journal of Nanobiotechnology* **20**(1), 395 (2022)
- [3] Monopoli, M.P., Åberg, C., Salvati, A., Dawson, K.A.: Biomolecular coronas provide the biological identity of nanosized materials. *Nature nanotechnology* **7**(12), 779–786 (2012)
- [4] Dawson, K.A., Yan, Y.: Current understanding of biological identity at the nanoscale and future prospects. *Nature Nanotechnology* **16**(3), 229–242 (2021)
- [5] Soddu, L., Trinh, D.N., Dunne, E., Kenny, D., Bernardini, G., Kokalari, I., Marucco, A., Monopoli, M.P., Fenoglio, I.: Identification of physicochemical properties that modulate nanoparticle aggregation in blood. *Beilstein journal of nanotechnology* **11**(1), 550–567 (2020)

- [6] Kamath, S., Lip, G.: Fibrinogen: biochemistry, epidemiology and determinants. *Qjm* **96**(10), 711–729 (2003)
- [7] Herrick, S., Blanc-Brude, O., Gray, A., Laurent, G.: Fibrinogen. *The international journal of biochemistry & cell biology* **31**(7), 741–746 (1999)
- [8] Weisel, J.W., Litvinov, R.I.: Fibrin formation, structure and properties. *Fibrous proteins: structures and mechanisms*, 405–456 (2017)
- [9] Mosesson, M.W., Siebenlist, K.R., Meh, D.A.: The structure and biological features of fibrinogen and fibrin. *Annals of the New York Academy of Sciences* **936**(1), 11–30 (2001)
- [10] Vilaseca, P., Dawson, K.A., Franzese, G.: Understanding and modulating the competitive surface-adsorption of proteins through coarse-grained molecular dynamics simulations. *Soft Matter* **9**(29), 6978–6985 (2013)
- [11] Xie, T., Chattoraj, J., Mulcahey, P.J., Kelleher, N.P., Del Gado, E., Hahn, J.-i.: Revealing the principal attributes of protein adsorption on block copolymer surfaces with direct experimental evidence at the single protein level. *Nanoscale* **10**(19), 9063–9076 (2018)
- [12] Vilanova, O., Mittag, J.J., Kelly, P.M., Milani, S., Dawson, K.A., Rädler, J.O., Franzese, G.: Understanding the kinetics of protein–nanoparticle corona formation. *ACS nano* **10**(12), 10842–10850 (2016)
- [13] McLoughlin, S.Y., Kastantin, M., Schwartz, D.K., Kaar, J.L.: Single-molecule resolution of protein structure and interfacial dynamics on biomaterial surfaces. *Proceedings of the National Academy of Sciences* **110**(48), 19396–19401 (2013) <https://doi.org/10.1073/pnas.1311761110> <https://www.pnas.org/content/110/48/19396.full.pdf>
- [14] Carnal, F., Clavier, A., Stoll, S.: Modelling the interaction processes between nanoparticles and biomacromolecules of variable hydrophobicity: Monte carlo simulations. *Environ. Sci.: Nano* **2**, 327–339 (2015) <https://doi.org/10.1039/C5EN00054H>
- [15] Kharazian, B., Lohse, S.E., Ghasemi, F., Raoufi, M., Saei, A.A., Hashemi, F., Farvadi, F., Alimohamadi, R., Jalali, S.A., Shokrgozar, M.A., Hadipour, N.L., Ejtehadi, M.R., Mahmoudi, M.: Bare surface of gold nanoparticle induces inflammation through unfolding of plasma fibrinogen. *Scientific Reports* **8**(1), 12557 (2018) <https://doi.org/10.1038/s41598-018-30915-7>
- [16] Guo, F., Luo, S., Wang, L., Wang, M., Wu, F., Wang, Y., Jiao, Y., Du, Y., Yang, Q., Yang, X., Yang, G.: Protein corona, influence on drug delivery system and its improvement strategy: A review. *International Journal of Biological Macromolecules* **256**, 128513 (2024) <https://doi.org/10.1016/j.ijbiomac.2023.128513>

- [17] March, D., Bianco, V., Franzese, G.: Protein unfolding and aggregation near a hydrophobic interface. *Polymers* **13**(1), 156 (2021)
- [18] Faulí, B.D., Bianco, V., Franzese, G.: Hydrophobic homopolymer’s coil–globule transition and adsorption onto a hydrophobic surface under different conditions. *The Journal of Physical Chemistry B* **127**(25), 5541–5552 (2023) <https://doi.org/10.1021/acs.jpcb.3c00937>
- [19] Asher, S.A.: Uv resonance raman spectroscopy for analytical, physical, and biophysical chemistry. part 1. *Analytical Chemistry* **65**(2), 59–66 (1993)
- [20] Fasman, G.D.: *Circular Dichroism and the Conformational Analysis of Biomolecules*. Springer, New York (1996)
- [21] Pignataro, M.F., Herrera, M.G., Dodero, V.I.: Evaluation of peptide/protein self-assembly and aggregation by spectroscopic methods. *Molecules* **25**(20), 1–35 (2020) <https://doi.org/10.3390/molecules25204854>
- [22] Asher, S.A., Ludwig, M., Johnson, C.R.: Uv resonance raman excitation profiles of the aromatic amino acids. *Journal of the American Chemical Society* **108**(12), 3186–3197 (1986)
- [23] Oladepo, S.A., Xiong, K., Hong, Z., Asher, S.A., Handen, J., Lednev, I.K.: Uv resonance raman investigations of peptide and protein structure and dynamics. *Chemical reviews* **112**(5), 2604–2628 (2012)
- [24] Miles, A.J., Janes, R.W., Wallace, B.A.: Tools and methods for circular dichroism spectroscopy of proteins: a tutorial review. *Chem. Soc. Rev.* **50**, 8400–8413 (2021) <https://doi.org/10.1039/D0CS00558D>
- [25] Micsonai, A., Moussong, É., Murvai, N., Tantos, Á., Töke, O., Réfrégiers, M., Wien, F., Kardos, J.: Disordered–ordered protein binary classification by circular dichroism spectroscopy. *Frontiers in Molecular Biosciences* **9**, 1–10 (2022)
- [26] Villani, C.: *Optimal Transport. Old and New*. Springer, Heildeberg (2008)
- [27] Peyré, G., Cuturi, M.: Computational optimal transport. *Foundations and Trends in Machine Learning* **11** (5-6), 355–602 (2019)
- [28] Hinton, G.E., Roweis, S.: Stochastic neighbor embedding. In: Becker, S., Thrun, S., Obermayer, K. (eds.) *Advances in Neural Information Processing Systems*, vol. 15. MIT Press, Boston, U.S.A (2002)
- [29] Maaten, L., Hinton, G.: Visualizing data using t-sne. *Journal of Machine Learning Research* **9**(86), 2579–2605 (2008)

- [30] Kobak, D., Berens, P.: The art of using t-sne for single-cell transcriptomics. *Nature Communications* **10**(1), 5416 (2019) <https://doi.org/10.1038/s41467-019-13056-x>
- [31] James, G., Witten, D., Hastie, T., Tibshirani, R., Friedman, J.: *The Elements of Statistical Learning with Applications in Python*. Springer Series in Statistics. Springer, New York, NY, USA (2023)
- [32] Porte, J., Herbst, B., Hereman, W., , Walt, S.: *Symposium of the Pattern Recognition*. PRASA, South Africa (2008)
- [33] Vershynin, R.: *High-dimensional Probability: An Introduction with Applications in Data Science*. Cambridge University Press, UK (2018)
- [34] Khan, S.S., Madden, M.G.: New similarity metrics for raman spectroscopy. *Chemometrics and Intelligent Laboratory Systems* **114**, 99–108 (2012) <https://doi.org/10.1016/j.chemolab.2012.03.007>
- [35] Jolliffe, I.T., Cadima, J.: Principal component analysis: a review and recent developments. *Philosophical Transactions of the Royal Society A: Mathematical, Physical and Engineering Sciences* **374**(2065), 20150202 (2016) <https://doi.org/10.1098/rsta.2015.0202> <https://royalsocietypublishing.org/doi/pdf/10.1098/rsta.2015.0202>
- [36] Deisenroth, M.P., Faisal, A.A., Ong, C.S.: *Mathematics for Machine Learning*. Cambridge University Press, Cambridge, UK (2020)
- [37] Kobak, D., Linderman, G.C.: Initialization is critical for preserving global data structure in both t-sne and umap. *Nature Biotechnology* **39**(2), 156–157 (2021) <https://doi.org/10.1038/s41587-020-00809-z>
- [38] Soliman, M.G., Martinez-Serra, A., Dobricic, M., Trinh, D.N., Cheeseman, J., Spencer, D.I., Monopoli, M.P.: Protocols for isolation and characterization of nanoparticle biomolecular corona complexes. *Frontiers in Toxicology* **6**, 1393330 (2024)
- [39] Dominguez-Medina, S., Kisley, L., Tauzin, L.J., Hoggard, A., Shuang, B., DS Indrasekara, A.S., Chen, S., Wang, L.-Y., Derry, P.J., Liopo, A., *et al.*: Adsorption and unfolding of a single protein triggers nanoparticle aggregation. *ACS nano* **10**(2), 2103–2112 (2016)
- [40] Ferreira, L.F., Picco, A.S., Galdino, F.E., Albuquerque, L.J.C., Berret, J.-F., Cardoso, M.B.: Nanoparticle–protein interaction: Demystifying the correlation between protein corona and aggregation phenomena. *ACS Applied Materials & Interfaces* **14**(25), 28559–28569 (2022) <https://doi.org/10.1021/acsami.2c05362> <https://doi.org/10.1021/acsami.2c05362>. PMID: 35696304

- [41] Domingues, M.M., Macrae, F.L., Duval, C., McPherson, H.R., Bridge, K.I., Ajjan, R.A., Ridger, V.C., Connell, S.D., Philippou, H., Ariëns, R.A.: Thrombin and fibrinogen γ' impact clot structure by marked effects on intrafibrillar structure and protofibril packing. *Blood, The Journal of the American Society of Hematology* **127**(4), 487–495 (2016)
- [42] Asamoto, D.K., Kim, J.E.: Uv resonance raman spectroscopy as a tool to probe membrane protein structure and dynamics. *Methods Mol Biol* **2003**, 327–349 (2019)
- [43] Oladepo, S.A., Xiong, K., Hong, Z., Asher, S.A.: Elucidating peptide and protein structure and dynamics: Uv resonance raman spectroscopy. *The journal of physical chemistry letters* **2**(4), 334–344 (2011)
- [44] Xu, M., Ermolenkov, V.V., Uversky, V.N., Lednev, I.K.: Hen egg white lysozyme fibrillation: a deep-uv resonance raman spectroscopic study. *Journal of biophotonics* **1**(3), 215–229 (2008)
- [45] Jakubek, R.S., Handen, J., White, S.E., Asher, S.A., Lednev, I.K.: Ultraviolet resonance raman spectroscopic markers for protein structure and dynamics. *TrAC Trends in Analytical Chemistry* **103**, 223–229 (2018)
- [46] Catalini, S., Rossi, B., Tortora, M., Foggi, P., Gessini, A., Masciovecchio, C., Bruni, F.: Hydrogen bonding and solvation of a proline-based peptide model in salt solutions. *Life* **11**(8), 824 (2021)
- [47] Catalini, S., Rossi, B., Foggi, P., Masciovecchio, C., Bruni, F.: Aqueous solvation of glutathione probed by uv resonance raman spectroscopy. *Journal of Molecular Liquids* **283**, 537–547 (2019)
- [48] Gómez, S., Bottari, C., Egidi, F., Giovannini, T., Rossi, B., Cappelli, C.: Amide spectral fingerprints are hydrogen bonding-mediated. *The Journal of Physical Chemistry Letters* **13**(26), 6200–6207 (2022)
- [49] Punihaole, D., Jakubek, R.S., Dahlburg, E.M., Hong, Z., Myshakina, N.S., Geib, S., Asher, S.A.: Uv resonance raman investigation of the aqueous solvation dependence of primary amide vibrations. *The Journal of Physical Chemistry B* **119**(10), 3931–3939 (2015)
- [50] Chi, Z., Asher, S.A.: Uv resonance raman determination of protein acid denaturation: selective unfolding of helical segments of horse myoglobin. *Biochemistry* **37**(9), 2865–2872 (1998)
- [51] Cho, N., Song, S., Asher, S.A.: Uv resonance raman and excited-state relaxation rate studies of hemoglobin. *Biochemistry* **33**(19), 5932–5941 (1994)

- [52] Miura, T., Takeuchi, H., Harada, I.: Tryptophan raman bands sensitive to hydrogen bonding and side-chain conformation. *Journal of Raman spectroscopy* **20**(10), 667–671 (1989)
- [53] Schlamadinger, D.E., Gable, J.E., Kim, J.E.: Hydrogen bonding and solvent polarity markers in the uv resonance raman spectrum of tryptophan: application to membrane proteins. *The Journal of Physical Chemistry B* **113**(44), 14769–14778 (2009)
- [54] Sanchez, K.M., Neary, T.J., Kim, J.E.: Ultraviolet resonance raman spectroscopy of folded and unfolded states of an integral membrane protein. *The Journal of Physical Chemistry B* **112**(31), 9507–9511 (2008)
- [55] Takeuchi, H.: Uv raman markers for structural analysis of aromatic side chains in proteins. *Analytical Sciences* **27**(11), 1077–1077 (2011)
- [56] Ahmed, Z., Beta, I.A., Mikhonin, A.V., Asher, S.A.: Uv- resonance raman thermal unfolding study of trp-cage shows that it is not a simple two-state miniprotein. *Journal of the American Chemical Society* **127**(31), 10943–10950 (2005)
- [57] Bianco, V., Franzese, G., Coluzza, I.: In silico evidence that protein unfolding is a precursor of protein aggregation. *ChemPhysChem* **21**(5), 377–384 (2020) <https://doi.org/10.1002/cphc.201900904>
- [58] Géron, A.: *Hands-On Machine Learning with Scikit-Learn and TensorFlow: Concepts, Tools, and Techniques to Build Intelligent Systems*. O’Reilly, U.S.A (2017)
- [59] Thorpe, M., Park, S., Kolouri, S., Rohde, G.K., Slepčev, D.: A transportation l distance for signal analysis. *Journal of Mathematical Imaging and Vision* **59**(2), 187–210 (2017)
- [60] Rousseeuw, P.J.: Silhouettes: A graphical aid to the interpretation and validation of cluster analysis. *Journal of Computational and Applied Mathematics* **20**, 53–65 (1987)
- [61] Kokalari, I., Gassino, R., Giovannozzi, A.M., Croin, L., Gazzano, E., Bergamaschi, E., Rossi, A.M., Perrone, G., Riganti, C., Ponti, J., *et al.*: Pro-and anti-oxidant properties of near-infrared (nir) light responsive carbon nanoparticles. *Free radical biology and medicine* **134**, 165–176 (2019)
- [62] D’amico, F., Saito, M., Bencivenga, F., Marsi, M., Gessini, A., Camisasca, G., Principi, E., Cucini, R., Di Fonzo, S., Battistoni, A., *et al.*: Uv resonant raman scattering facility at elettra. *Nuclear Instruments and Methods in Physics Research Section A: Accelerators, Spectrometers, Detectors and Associated Equipment* **703**, 33–37 (2013)

- [63] Guo, S., Popp, J., Bocklitz, T.: Chemometric analysis in raman spectroscopy from experimental design to machine learning-based modeling. *Nat Protoc* **16**, 5426–5459 (2021)
- [64] Micsonai, A., Moussong, É., Wien, F., Boros, E., Vadász, H., Murvai, N., Lee, Y.-H., Molnár, T., Réfrégiers, M., Goto, Y., Tantos, Á., Kardos, J.: BeStSel: webserver for secondary structure and fold prediction for protein CD spectroscopy. *Nucleic Acids Research* **50**(W1), 90–98 (2022) <https://doi.org/10.1093/nar/gkac345> https://academic.oup.com/nar/article-pdf/50/W1/W90/44378198/gkac345_supplemental_file.pdf
- [65] Rasmussen, C.E., Williams, K.I.: *Gaussian Processes for Machine Learning*. MIT Press, Boston, U.S.A (2006)
- [66] Duvenaud, D., Lloyd, J., Grosse, R., Tenenbaum, J., Zoubin, G.: Structure discovery in nonparametric regression through compositional kernel search. In: Dasgupta, S., McAllester, D. (eds.) *Proceedings of the 30th International Conference on Machine Learning*. *Proceedings of Machine Learning Research*, vol. 28, pp. 1166–1174. PMLR, Atlanta, Georgia, USA (2013)
- [67] Monge, G.: *Mémoire sur la théorie des déblais et des remblais*. De l’Imprimerie Royale (1781)
- [68] Kantorovich, L.V.: A problem of monge. *Uspekhi Mat. Nauk* **3**(24):225–226 (1948)
- [69] Kantorovich, L.V.: Mathematical methods of organizing and planning production. *Management Science* **6**(4):366–422 (1960)
- [70] Prugel-Bennett, A.: *The Probability Companion for Engineering and Computer Science*. Cambridge University Press, Cambridge, UK (2020)
- [71] Virtanen, P., Gommers, R., Oliphant, T.E., Haberland, M., Reddy, T., Cournapeau, D., Burovski, E., Peterson, P., Weckesser, W., Bright, J., van der Walt, S.J., Brett, M., Wilson, J., Millman, K.J., Mayorov, N., Nelson, A.R.J., Jones, E., Kern, R., Larson, E., Carey, C.J., Polat, İ., Feng, Y., Moore, E.W., VanderPlas, J., Laxalde, D., Perktold, J., Cimrman, R., Henriksen, I., Quintero, E.A., Harris, C.R., Archibald, A.M., Ribeiro, A.H., Pedregosa, F., van Mulbregt, P., SciPy 1.0 Contributors: SciPy 1.0: Fundamental Algorithms for Scientific Computing in Python. *Nature Methods* **17**, 261–272 (2020) <https://doi.org/10.1038/s41592-019-0686-2>